INTERNATIONAL JOURNAL FOR NUMERICAL METHODS IN FLUIDS, VOL. 12, 895–908 (1991)

UNSTEADY FLOW CALCULATION IN A RADIAL FLOW CENTRIFUGAL PUMP WITH SPIRAL CASING

EVANGELOS E. MORFIADAKIS, SPYROS G. VOUTSINAS AND DIMITRIS E. PAPANTONIS

Department of Mechanical Engineering, National Technical University of Athens, 42, 28th October Str., 106 82 Athens, Greece

SUMMARY

The prediction of the two-dimensional unsteady flow established in a radial flow centrifugal pump is considered. Assuming the fluid incompressible and inviscid, the velocity field is represented by means of source and vorticity surface distributions as well as a set of point vortices. Using this representation, a grid-free (Lagrangian) numerical method is derived based on the coupling of the boundary element and vortex particle methods. In this context the source and vorticity surface distributions are determined through the non-entry boundary condition together with the unsteady Kutta condition. In order to satisfy Kelvin's theorem, vorticity is shed at the trailing edges of the impeller blades. Then the vortex particle method is used to approximate the convection of the free vorticity distribution. Results are given for a pump configuration experimentally tested by Centre Technique des Industries Mécaniques (CETIM). Comparisons between predictions and experimental data show the capability of the proposed method to reproduce the main features of the flow considered.

KEY WORDS Unsteady flow Vortex method Boundary element method Centrifugal pump Spiral casing

INTRODUCTION

Among the various engineering applications amenable to CFD analysis, those with moving boundaries constitute a more or less distinct category. A typical example of this kind, to be considered in the present paper, is the flow within a pump. For a pump configuration the moving boundaries are the blades of the impeller which rotate with respect to the spiral casing.

The full mathematical problem describing flows with moving boundaries is clearly the unsteady problem for the Navier–Stokes equations. In order to solve this problem numerically, we can use either Eulerian or Lagrangian methods. In the first case a spatial grid throughout the flow field is required. However, the presence of moving boundaries calls for special treatment leading to considerable computational effort. In the framework of the viscous flow theory, recently Kueny and Papantonis[1] presented numerical results for the unsteady flow within the spiral casing. These results were obtained by means of a finite volume numerical scheme on a fixed grid limited by the exit section of the impeller. The unsteadiness of the flow was introduced through the boundary conditions along the exit section of the impeller. More specifically, a non-uniform rotating profile of the absolute velocity is considered. However, the replacement of the impeller by a rotating profile is a crude approximation of the interaction between the impeller and the spiral casing. This approximation can give misleading results, especially under off-design operation conditions. Evidently, in order to improve the accuracy of the numerical results, the solution domain must be extended within the region of the impeller. In this case the exit section of the impeller becomes a matching boundary where continuity conditions are imposed. This is by

0271–2091/91/090895–14$07.00

Received January 1990
Revised June 1990

no means a trivial task since matching conditions must take into account the flux of vorticity across the exit section of the impeller.

In contrast, Lagrangian methods and especially vortex particle methods are grid-free and thus preferable for flows with moving boundaries. However, while moving boundaries are easily tackled, the fulfilment of the no-slip condition is not straightforward. In the context of fully Lagrangian methods this condition is satisfied by a vorticity generation process all along the solid boundaries. As reported in the literature,[2,3] in order to obtain a good approximation, a large number of vortex particles are required. Obviously, for complicated configurations such as that of a pump, reliable predictions can be produced only with considerable computer resources. On the other hand, under the hypothesis of an inviscid fluid, most of the disadvantages of the Lagrangian methods no longer exist. As explained in the following sections, in this context a general method can be derived with no need for additional simplifying assumptions.

All previous relevant works introduce either geometrical or physical simplifications. More specifically, in the works presented by Albano,[4] Hureau[5] and Devinant *et al.*[6] the blades are considered of zero thickness and the flow irrotational. Thus no vortex shedding at the trailing edges of the impeller blades takes place. Consequently this is a rather quasi-steady approximation of the flow. A more realistic approach was given by Shoji and Ohashi[7]. In that work the problem of a single impeller whirling on a circular orbit is considered. Although the blades still remain thin, vorticity shedding is introduced.

As already mentioned, for the inviscid case a general fully Lagrangian method can be derived. The method is based on the combined application of Helmholtz's and Green's theorems. As a result, a representation theorem for the velocity field is obtained. According to this theorem, the velocity field is expressed uniquely by means of source and vorticity surface distributions as well as by means of a set of point vortices. The source and vorticity distributions are determined through the non-entry boundary condition and the Kutta condition. Since the flow is unsteady, it follows from Kelvin's theorem that vorticity is shed at the trailing edges of the blades of the impeller. Through this process, free vorticity is produced. Clearly all fluid particles carrying vorticity will be convected along the trajectories of the flow field.

The approach just outlined is closely related to the method used by Basu and Hancock[8] for the unsteady flow around an aerofoil (for a discussion on the unsteady Kutta condition see also References 9–11).

In order to validate the proposed method, results are given in the last section of the present paper for a centrifugal pump experimentally tested by CETIM. Comparisons show that the predicted variation of the head versus the flow rate is in very good agreement with the corresponding experimental data, while the details of the flow seem well reproduced at least qualitatively.

THE UNSTEADY FLOW FIELD

For a two-dimensional approach to the problem, the flow field considered is as in Figure 1. D denotes the domain occupied by the fluid with boundary ∂D consisting of the spiral casing C, the exit section S_0 and the rotor blades S_i, $i = 1(1)N_b$.

The flow examined in the sequel is the unsteady flow generated by the rotation of the rotor blades at angular velocity ω_R. For a centrifugal pump the rotation of the rotor results in an inflow across the inlet section. Let $Q(t)$ denote the flow rate, represented as a first approximation by a point source located at the centre O of the rotor. Assuming the fluid incompressible and inviscid, the main feature of the flow considered is the non-zero circulation around every rotor blade. In the context of unsteady flow theory the circulation around a moving solid boundary is time-

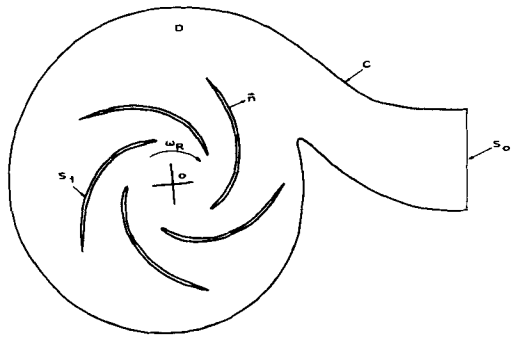

Figure 1. Definition of the physical domain

dependent. This fact combined with Kelvin's theorem leads to the necessity of vorticity shedding from the trailing edges of the rotor blades. Consequently the velocity field is no longer irrotational.

Under the above assumptions and according to the Helmholtz decomposition theorem the velocity field $\mathbf{u}(\mathbf{x}; t)$ is given by

$$\mathbf{u}(\mathbf{x}; t) = \nabla\varphi(\mathbf{x}; t) + \nabla \wedge \psi(\mathbf{x}; t), \tag{1}$$

where $\varphi(\cdot; t)$ and $\psi(\cdot; t)$ denote the scalar potential and the streamfunction repectively. Taking the divergence and curl of (1), we deduce

$$\nabla^2\varphi(\mathbf{x}; t) = Q(t)\delta(\mathbf{x}), \tag{2}$$

$$\nabla^2\psi(\mathbf{x}; t) = -\omega(\mathbf{x}; t), \tag{3}$$

where $\omega(\cdot; t)$ denotes the free vorticity distribution and $\delta(\cdot)$ the Dirac function. If $\varphi(\cdot; t)$ and $\psi(\cdot; t)$ are continuous in $D \cup \partial D$, by means of Green's theorem we obtain

$$\varphi(\mathbf{x}; t) = Q(t)G(\mathbf{x}) + \int_{\partial D} \sigma(\mathbf{y}; t)G(\mathbf{x} - \mathbf{y})\mathrm{d}S(\mathbf{y}), \tag{4}$$

$$\psi(\mathbf{x}; t) = -\int_D \omega(\mathbf{y}; t)G(\mathbf{x} - \mathbf{y})\mathrm{d}D(\mathbf{y}) + \int_{\partial D} \gamma(\mathbf{y}; t)G(\mathbf{x} - \mathbf{y})\mathrm{d}S(\mathbf{y}), \tag{5}$$

where $\sigma(\cdot; t)$ denotes the source distribution, $\gamma(\cdot; t)$ the bound vorticity distribution and $G(\cdot)$ the singular solution of the Laplace equation. It follows from (1)–(5) that $\mathbf{u}(\cdot; t)$ is fully determined if $\sigma(\cdot; t)$, $\gamma(\cdot; t)$ and $\omega(\cdot; t)$ are given. In this direction appropriate conditions are imposed for the three auxiliary distributions $\sigma(\cdot; t)$, $\gamma(\cdot; t)$ and $\omega(\cdot; t)$.

For an inviscid fluid the only kinematical boundary conditions available is the non-entry condition along ∂D. More specifically,

$$g(\mathbf{x}; t) = \mathbf{u}(\mathbf{x}; t)\cdot\mathbf{n}(\mathbf{x}) = \begin{cases} \omega_R(\mathbf{n}(\mathbf{x}; t) \wedge \mathbf{x}(t)), & \mathbf{x}(t) \in S_i(t), \quad i = 1(1)N_b, \\ 0, & \mathbf{x} \in C, \\ -Q(t)/L_0, & \mathbf{x} \in S_0, \end{cases} \tag{6}$$

where $\mathbf{n}(\cdot; t)$ denotes the unit normal as in Figure 1. This condition can be used to determine either $\varphi(\cdot; t)$ or $\psi(\cdot; t)$. The form of representation of $\varphi(\cdot; t)$ suggests using this condition as a Neumann condition for the evaluation of the source distribution. Inserting (4) and (5) in (1) and

then in (6), we derive an integral boundary relation of the form

$$\pi\sigma(\mathbf{x};t)+\mathbf{n}(\mathbf{x};t)\cdot\int_{\partial D}\sigma(\mathbf{y};t)\frac{\mathbf{x}-\mathbf{y}}{|\mathbf{x}-\mathbf{y}|^2}\,\mathrm{d}S(\mathbf{y})+\mathbf{n}(\mathbf{x};t)\wedge\int_{\partial D}\gamma(\mathbf{y};t)\frac{\mathbf{x}-\mathbf{y}}{|\mathbf{x}-\mathbf{y}|^2}\,\mathrm{d}S(\mathbf{y})$$
$$=-Q(t)\mathbf{n}(\mathbf{x};t)\frac{\mathbf{x}}{|\mathbf{x}|^2}+\mathbf{n}(\mathbf{x};t)\wedge\int_D\omega(\mathbf{y};t)\frac{\mathbf{x}-\mathbf{y}}{|\mathbf{x}-\mathbf{y}|^2}\,\mathrm{d}D(\mathbf{y})+2\pi g(\mathbf{x};t). \tag{7}$$

This relation can be interpreted as a Fredholm integral equation of the second kind for $\sigma(\cdot;t)$. Since there is no other kinematical condition, the streamfunction can be determined only through dynamical conditions concerning the vorticity shedding.

In this direction we assume non-zero bound vorticity $\gamma(\cdot;t)$ only along the rotor blades. Moreover, for every blade, $\gamma(\cdot;t)$ is taken as constant. Thus

$$\int_{S_i}\gamma(y;t)\mathrm{d}S(\mathbf{y})=\gamma_i(t)L_i=\Gamma_i(t), \tag{8}$$

where L_i denotes the length of $S_i(t)$ and $\Gamma_i(t)$ the circulation around the ith blade at time t. As explained in the sequel, the evaluation of the circulations Γ_i is based on a suitable application of the Kutta condition. In order to complete the determination of the streamfunction, a model for the vorticity production is required. Through this model we can give to $\omega(\cdot;t)$ an explicit description.

Following the analysis of Mangler and Smith[12] (see also References 8 and 13), the vorticity at the trailing edge of a blade is shed tangentially to either one of the two sides of the wedge formed, according to the sign of the circulation around the blade (Figure 2). This process results in the formation of a thin vortex sheet that models the wake of the blade in the framework of inviscid flow theory. Let $w_i^+(t)$ and $w_i^-(t)$ denote the velocities relative to the blade at the two sides of the trailing edge, $\gamma_{wi}(t)$ the intensity of the vortex sheet and $\mathrm{d}l_{wi}(t)$ the length produced in a time interval $\mathrm{d}t$. Since the surface vorticity is equivalent to a tangential velocity jump,

$$\gamma_{wi}(t)=w_i^+(t)-w_i^-(t). \tag{9}$$

Moreover, from Kelvin's theorem we obtain

$$\mathrm{d}\Gamma_i(t)=\Gamma_i(t+\mathrm{d}t)-\Gamma_i(t)=\gamma_{wi}(t)\mathrm{d}l_{wi}(t), \tag{10}$$

where

$$\mathrm{d}l_{wi}(t)=\tfrac{1}{2}[w_i^+(t)+w_i^-(t)]\,\mathrm{d}t=w_i(t)\mathrm{d}t. \tag{11}$$

Combining (9)–(11), we can obtain a non-linear evolution equation for $\Gamma_i(t)$:

$$\frac{\mathrm{d}\Gamma_i(t)}{\mathrm{d}t}=\tfrac{1}{2}[w_i^+(t)+w_i^-(t)][w_i^+(t)-w_i^-(t)]. \tag{12}$$

This condition is often called the unsteady Kutta condition.[9]

Figure 2. Vortex sheet shedding from the trailing edge of the blade

In accordance with the above description, the free vorticity distribution is the sum of N_b vortex sheets $S_{w_i}(t)$. Let $\mathbf{Z}_i(\tau; t)$ denote the position of a point on $S_{w_i}(t)$ at time t that was emitted from the ith blade at time τ. It follows that

$$\omega(\mathbf{x}; t) = \sum_{i=1}^{N_b} \gamma_{wi}(\tau)\, \delta(\mathbf{x} - \mathbf{Z}_i(\tau; t)), \tag{13}$$

$$\frac{d\mathbf{Z}_i(\tau; t)}{dt} = \mathbf{u}(\mathbf{Z}_i(\tau; t); t), \tag{14}$$

with initial conditions

$$\gamma_{wi}(0) = 0, \qquad \mathbf{Z}_i(\tau; 0) = \mathbf{x}_{TE}(\tau), \tag{15}$$

where $\mathbf{x}_{TE}(\tau)$ denotes the position of the trailing edge of the ith blade at time τ.

From the above analysis we finally obtain the following representation for the streamfunction:

$$\psi(\mathbf{x}; t) = \sum_{i=1}^{N_b} \left(\frac{\Gamma_i(t)}{L_i} \int_{S_i} G(\mathbf{x} - \mathbf{y}) dS(\mathbf{y}) + \int_0^t \gamma_{wi}(\tau) G(\mathbf{x} - \mathbf{Z}_i(\tau; t)) \left| \frac{d\mathbf{Z}_i(\tau; t)}{d\tau} \right| d\tau \right). \tag{16}$$

Equation (7) for the source distribution together with equation (12) for the blade circulations and equations (10), (11), (14) and (15) for the evolution of the vortex sheets S_{wi} define the problem to be solved.

THE NUMERICAL METHOD

In order to numerically solve the problem formulated in the previous section, a time-marching scheme is proposed with time step Δt. Using the notation

$$a(\mathbf{x}; k\Delta t) = a^{(k)}(\mathbf{x}) \tag{17}$$

for all time-dependent variables, for every time step $k = 0, 1, \ldots$, given the solution at $t = k\Delta t$, the algorithm will determine the solution at $t = (k + 1)\Delta t$. The realization of this process is based on the boundary element dicretization for equation (7) and the vortex particle approximation for the N_b vortex sheets. In this direction the boundary ∂D is divided into flat elements S_e, $e = 1(1)E$, carrying a constant source distribution. Especially for the elements forming the rotor blades a constant vorticity distribution is added. If equation (7) is satisfied for all midpoints $\mathbf{x}_{e,m}^{(k)}$ of the boundary elements, a set of linear equations with respect to the source intensities $\sigma_e^{(k)}$, $e = 1(1)E$, is obtained. Clearly this system depends on the approximation of the blade wakes. In the context of the vortex particle method the free vorticity is given as a sum of point vortices. For the problem considered during a time step j, N_b vortex segments $\Delta S_{wi}^{(j)}$ carrying constant vorticity distributions $\gamma_{wi}^{(j)}$ are shed. These segments are transformed into point vortices when convected for the first time. Let Ω_i^j and $\mathbf{Z}_i^{j(j)}$ denote the intensity and position of the corresponding point vortex. Using (10) and according to Kelvin's theorem,

$$\Omega_i^j = \Gamma_i^j - \Gamma_i^{j-1}. \tag{18}$$

Since $\gamma_{wi}^{(j)}$ is constant, a consistent choice for $\mathbf{Z}_i^{j(j)}$ is the midpoint of $\Delta S_{wi}^{(j)}$. Clearly with this choice as initial condition,

$$\mathbf{Z}_i^{j(k+1)} = \mathbf{Z}_i^{j(k)} + \Delta t\, \mathbf{u}^{(k)}(\mathbf{Z}_i^{j(k)}). \tag{19}$$

Under the above assumptions, $\omega^{(k+1)}(\mathbf{x})$ is given by

$$\omega^{(k+1)}(\mathbf{x}) = \sum_{i=1}^{N_b} \left(\gamma_{wi}^{(k+1)} \delta(\mathbf{x}; \Delta S_{wi}^{(k+1)}) + \sum_{j=1}^{k} \Omega_i^j \, \delta(\mathbf{x} - \mathbf{Z}_i^{j(k+1)}) \right), \tag{20}$$

where

$$\delta(\mathbf{x}; \Delta S_{wi}^{(j)}) = \begin{cases} 1 & \text{if } \mathbf{x} \in \Delta S_{wi}^{(j)}, \\ 0 & \text{otherwise.} \end{cases} \tag{21}$$

Therefore equations (7), (9) and (10) lead to the following system:

$$[A^{(k+1)}]\{\sigma^{(k+1)}\} + [B^{(k+1)}]\{\Gamma^{(k+1)}\} = \{b^{(k+1)}\}, \tag{22}$$

where

$$A_{e,e'}^{(k)} = \mathbf{n}_e^{(k)} \cdot \int_{S_{e'}} \frac{\mathbf{x}_{e,\mathrm{m}}^{(k)} - \mathbf{x}}{|\mathbf{x}_{e,\mathrm{m}}^{(k)} - \mathbf{x}|^2} \, \mathrm{d}S,$$

$$B_{e,i}^{(k)} = \mathbf{n}_e^{(k)} \wedge \frac{1}{L_i} \int_{S_i} \frac{\mathbf{x}_{e,\mathrm{m}}^{(k)} - \mathbf{x}}{|\mathbf{x}_{e,\mathrm{m}}^{(k)} - \mathbf{x}|^2} \, \mathrm{d}S,$$

$$b_e^{(k)} = -Q^{(l)} \frac{\mathbf{n}_e^{(k)} \cdot \mathbf{x}_{e,\mathrm{m}}^{(k)}}{|\mathbf{x}_{e,\mathrm{m}}^{(k)}|^2} + \mathbf{n}_e^{(k)} \wedge \sum_{i=1}^{N_b} \sum_{j=1}^{k-1} \Omega_i^j \frac{\mathbf{x}_{e,\mathrm{m}}^{(k)} - \mathbf{Z}_{ij}^{(k)}}{|\mathbf{x}_{e,\mathrm{m}}^{(k)} - \mathbf{Z}_{ij}^{(k)}|^2} + 2\pi g(\mathbf{x}_{e,\mathrm{m}}^{(k)}),$$

$$\{\sigma^{(k)}\} = \{\sigma_1^{(k)}, \sigma_2^{(k)}, \ldots, \sigma_E^{(k)}\}^{\mathrm{T}},$$

$$\{\Gamma^{(k)}\} = \{\Gamma_1^{(k)}, \Gamma_2^{(k)}, \ldots, \Gamma_{N_b}^{(k)}\}^{\mathrm{T}}.$$

If the geometry (i.e. the length and direction of $\Delta S_{wi}^{(k+1)}$) of the vortex sheets is given, then (22) is a linear system with respect to $\{\sigma^{(k+1)}\}$ and $\{\Gamma^{(k+1)}\}$.

Having completed the description of the approximations introduced, we proceed with the substeps comprising a full time step. Starting at the kth step, we are placed at time $t = k\Delta t$. Then:

1. *Convection substep.* All point vortices together with the free vortex segments are convected using (19). At their new positions the free vortex segments are transformed into vortex particles according to (18).
2. *Initialization substep.* Using the velocity field $\mathbf{u}^{(k)}$, the length and direction of the vortex segment to be emitted at $t = (k+1)\Delta t$ are defined.
3. *Iterative procedure*
   - 3.1. Solving the linear system (22), the source distribution as well as the circulations around the blades are determined.
   - 3.2. The geometry of the new vortex segments is corrected.
   - 3.3. If convergence is accomplished, we proceed to the next step; otherwise we repeat 3.1 and 3.2.

We conclude the description of the method with two remarks related to the convection step. The first concerns the calculation of the velocity induced by a point vortex. Owing to the singular behaviour of $G(\cdot)$ and its derivatives, we regularize the induced velocity by means of a cut-off function.[14, 15] A rather frequent choice is the exponential function defining the Rankine vortex. Selecting this cut-off function, the regularized velocity at $\mathbf{x}$ induced by a point vortex of intensity

Ω located at $\mathbf{y}$ takes the form

$$\mathbf{u}(\mathbf{x}) = \frac{\Omega}{2\pi}\mathbf{k} \wedge \frac{\mathbf{x}-\mathbf{y}}{|\mathbf{x}-\mathbf{y}|^2}\left[1 - \exp\left(\frac{|\mathbf{x}-\mathbf{y}|^2}{\varepsilon^2}\right)\right], \tag{23}$$

where ε is the cut-off length. The second remark concerns the convection itself. Clearly, as point vortices are convected, even for relatively small Δt, it is probable that a vortex will pass across the boundary ∂D. This can happen only in the vicinity of ∂D, where length scales present a quick variation. In order to account for this local behaviour, either a smaller time step or a higher-order scheme is required. In both cases the computational cost increases. In order to keep the computational cost reasonable, we preferred a simple correction. Thus the vortices that fall outside D are simply moved back in D symmetrically with respect to the ∂D positions.

RESULTS AND DISCUSSION

In order to validate the method given in the previous section, numerical tests were conducted for a centrifugal pump experimentally tested by CETIM.[16] The main characteristics of this pump are given in Table I. The volute is designed according to the moment of momentum conservation principle. The inlet and outlet edges of the impeller blades are parallel to the axis of rotation.

For the boundary element approximation, 96 elements were used along the spiral casing, six elements along the exit section S_0 and 40 elements along every blade. In order to improve the approximation of the flow field, the repartition of elements is refined in regions where sharp local gradients are expected. For the configuration considered, refinement is necessary around the tongue as well as around the trailing and leading edges of the blades.

The time step was taken as $\Delta t = T/60$, where $T = 2\pi/\omega$ is the period of the rotation. Since the number of blades is equal to five and ω_R is constant, $12\Delta t$ is the time interval required for a blade to move to the position the following blade had at the beginning of this interval. Therefore the flow is expected to tend to become periodic with period $T/5$. This feature has been verified numerically.

In the sequel, results are presented for four different values of the flow rate $Q{:}Q/Q_n = 0{\cdot}47$, $0{\cdot}706$, $1{\cdot}0$ and $1{\cdot}41$, with Q_n denoting the flow rate at the best efficiency. According to the experimental data for the pump running at $n = 1000$ rpm, Q_n is equal to $85\ \mathrm{m^3\,h^{-1}}$.

In Figure 3 the positions of the free vortices are given at $t = 92\Delta t$, i.e. after $1{\cdot}5$ rotations of the impeller, for the four values of the flow rate. Considering that the flow is impulsively started, the

Table I. The main characteristics of the CETIM pump

Inner diameter of the impeller	$d_1 = 0{\cdot}134$ m
Outer diameter of the impeller	$d_2 = 0{\cdot}310$ m
Inclination of the blades at the inner diameter	$\beta_1 = 22{\cdot}3°$
Inclination of the blades at the outer diameter	$\beta_2 = 30{\cdot}0°$
Width of the impeller at the inlet diameter	$b_1 = 0{\cdot}030$ m
Width of the impeller at the outlet diameter	$b_2 = 0{\cdot}0145$ m
Number of blades	$N_b = 5$
Position of the tongue	$\alpha_t = 9°$
Volute angle	$\alpha_v = 9{\cdot}5°$
Ratio of throat area A_t to outlet area A_2	$A_t/A_2 = 1{\cdot}20$
Ratio of exit area A_0 to outlet area A_2	$A_0/A_2 = 0{\cdot}60$
Speed of rotation of the impeller	$n = 1000$ rpm
Angular velocity	$\omega_R = 104{\cdot}72\ \mathrm{rad\,s^{-1}}$

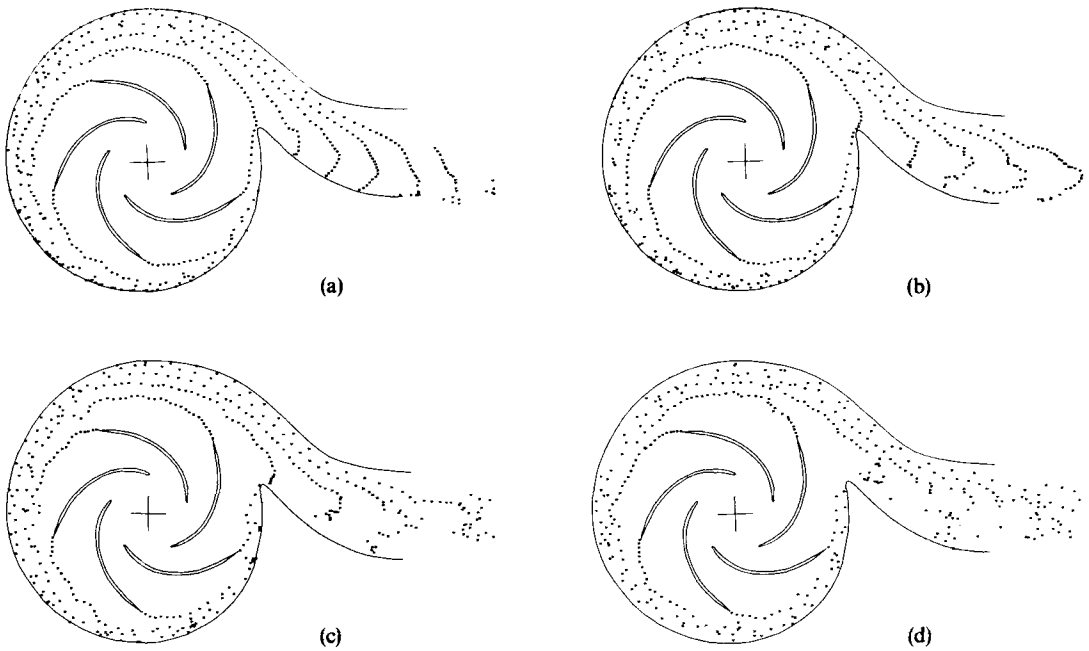

Figure 3. Position of the free vortices at $t = 92\Delta t$: (a) $Q/Q_n = 0{\cdot}47$; (b) $Q/Q_n = 0{\cdot}706$; (c) $Q/Q_n = 1{\cdot}0$; (d) $Q/Q_n = 1{\cdot}41$

initial vortices carry a large amount of vorticity. Thus the flow can be considered well developed as soon as these vortices are convected outside the exit section S_0 and so their contribution to the flow field inside the casing is small. This is clearly shown in Figure 3. On the other hand, we notice that inside the spiral casing the vortices are almost uniformly distributed in accordance with the non-uniform character of the velocity field. In contrast, in the exit channel of the casing, downstream from the tongue of the casing, the vortices retain their organized structure since the flow field is more uniform there and no important interaction between the vortices takes place. Of course, as the flow rate increases, the shear in the exit channel increases as well and so the structure of the vorticity distribution therein is less organized.

The positions of the free vortices shed from the blades for the case of Q_n and for $t = 5\Delta t$ and $8\Delta t$ are given in Figures 4(a) and 4(b) respectively. It is interesting to notice that the first vortices shed by the blade located just after the tongue are convected into the exit channel directly, forming the organized structures shown in Figure 3. On the other hand, the other vortices have to do an almost complete rotation into the spiral casing before arriving in the exit channel.

The vector diagrams of the absolute velocity into the spiral casing at $t = 92\Delta t$ are given in Figure 5 for the four selected values of the flow rate. The stagnation point for $Q/Q_n = 0{\cdot}47$ and $0{\cdot}706$ is well located on the tongue of the casing and therefore the flow field is more regular there. As the flow rate increases, the stagnation point of the casing moves towards the lower surface of the tongue, as expected. This results in a less regular flow field. In conclusion, the best flow rate for the considered spiral casing is between $0{\cdot}47Q_n$ and $0{\cdot}706Q_n$. This result can be explained by the fact that the real spiral casing is not two-dimensional and its width in the axial direction increases in order to reduce the overall dimensions of the casing. On the other hand, if for the needs for the numerical solution the radial sections of the casing were increased in order to satisfy mass conservation, the moment of momentum principle could no longer be satisfied.

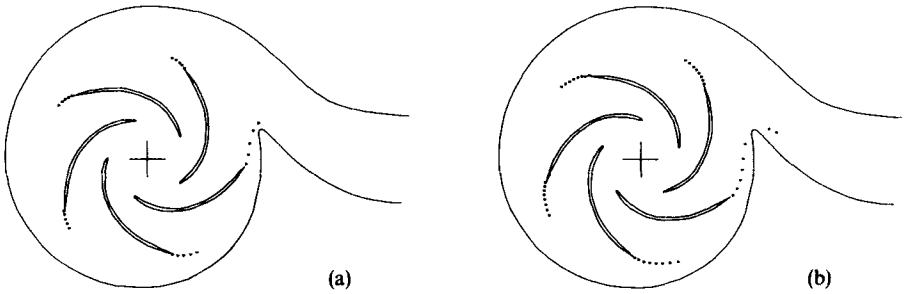

Figure 4. Position of the free vortices for $Q = Q_n$ at time steps $5\Delta t$ and $8\Delta t$

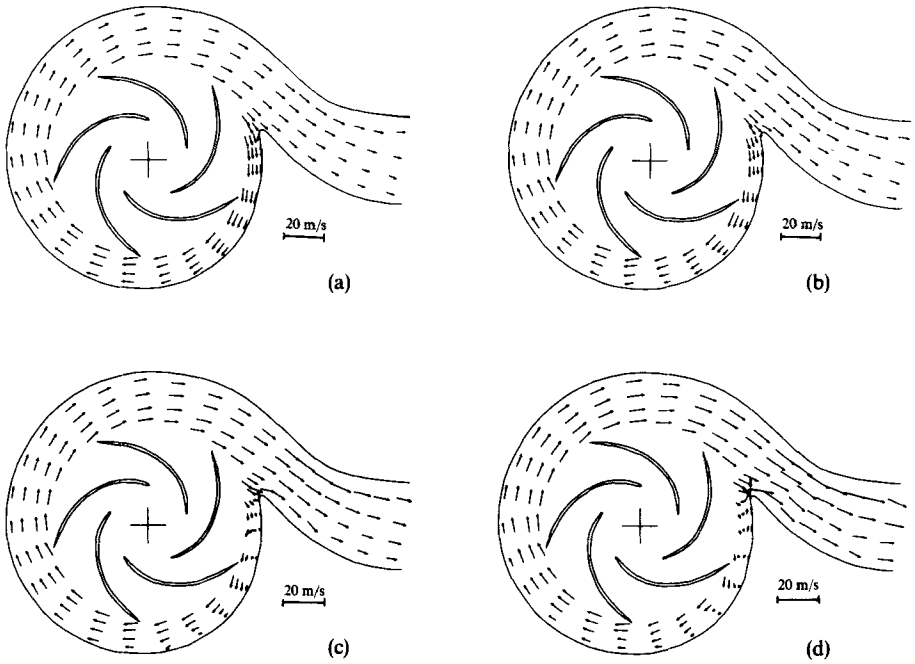

Figure 5. Vector diagram of the absolute velocity into the spiral casing at $t = 92\Delta t$: (a) $Q/Q_n = 0{\cdot}47$; (b) $Q/Q_n = 0{\cdot}706$; (c) $Q/Q_n = 1{\cdot}0$; (d) $Q/Q_n = 1{\cdot}41$

The vector diagrams of the relative velocity between the blades at $t = 92\Delta t$ for the four selected values of the flow rate are given in Figure 6. For the smaller values of the flow rate the recirculation of the relative flow between the blades is more pronounced, while the centre of the recirculation region moves towards the outer diameter of the impeller as the flow rate increases. For $Q/Q_n = 1{\cdot}0$ the inclination of the relative velocity at the input section of the impeller seems to be well adapted to the corresponding inclination of the blades. In contrast, for the smaller values of the flow rate a negative angle of incidence appears at the leading edge of the blades. For the selected values of the flow rate the relative flow is almost identical for all the blade-to-blade channels with the exception of the one located against the tongue of the casing. In this last case the recirculation region is less pronounced or even non-existent (for $Q/Q_n = 1{\cdot}0$ and $1{\cdot}41$). This

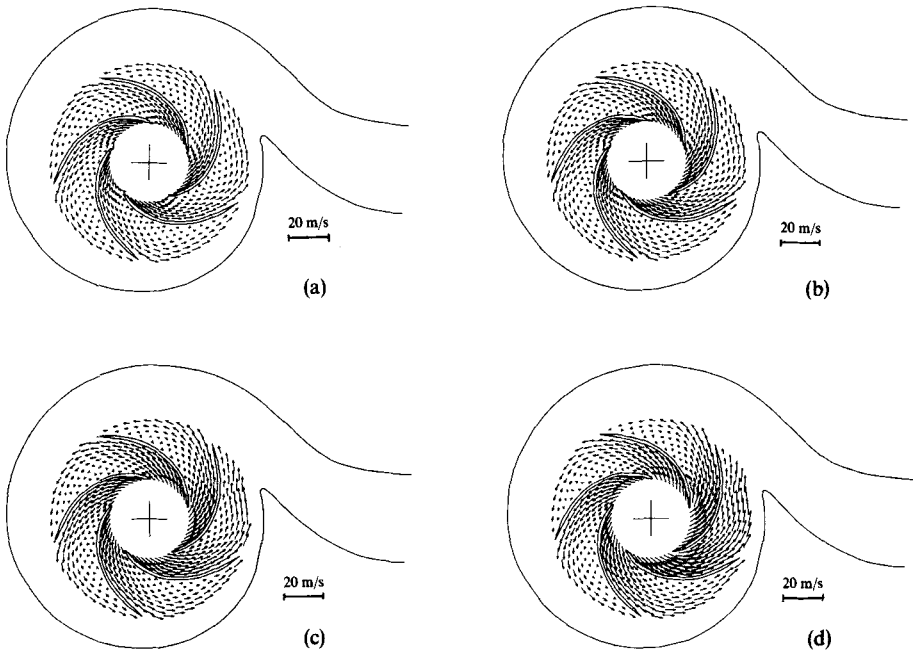

Figure 6. Vector diagram of the relative velocity between the blades at $t = 92\Delta t$: (a) $Q/Q_n = 0{\cdot}47$; (b) $Q/Q_n = 0{\cdot}706$; (c) $Q/Q_n = 1{\cdot}0$; (d) $Q/Q_n = 1{\cdot}41$

phenomenon is expected since this blade-to-blade channel discharges almost directly to the exit channel of the casing. Consequently the crossing flow rate is more important compared to the other blade-to-blade channels and the blades are less loaded when passing from the tongue.

At the exit section of the impeller the flow conditions are not uniform owing to the wakes of the blades and the non-axisymmetric configuration of the spiral casing. This last non-axisymmetry is expected to be more important in the vicinity of the tongue, where the distance between the blades and the tongue is a minimum. This effect is shown in Figures 7(a) and 7(b) for $Q/Q_n = 0{\cdot}47$ and $0{\cdot}706$ respectively, where the radial component of the absolute velocity around the impeller's outer diameter is plotted. Position 1 on the horizontal axis corresponds to the location of the tongue, while on the whole perimeter of 360°, 120 points are considered. The triangles located on the horizontal axis ($c_r = 0$) indicate the position of the blade trailing edges at $t = 92\Delta t$. The solid line corresponds to the impeller alone, i.e. without the spiral casing, and for this reason it is perfectly periodic. It follows from both physical considerations and experimental data[17] that the formation of the blade wakes results in a local sharp increase of the radial component of the velocity. Since the fluid is directly guided by the blades, this non-uniform profile is rotating unchanged with the impeller. The dashed line gives the calculated radial component around the outer perimeter of the impeller with the spiral casing taken into account as well. Comparison of these two curves indicates the influence of the spiral casing. Clearly the influence becomes more important in the vicinity of the tongue.

The unsteady periodic character of the flow is also displayed in the time variation of the moment developed. The moment from the axis of rotation on every blade is calculated by means of the Bernoulli equation. From the total moment developed to all the blades, i.e. on the impeller, the theoretical head H_u of the impeller is then calculated. We consider a full period corresponding

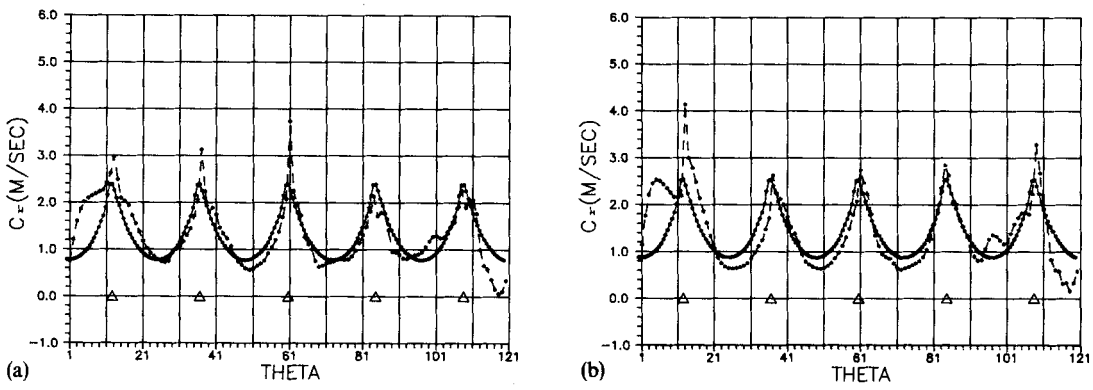

Figure 7. Radial component of the absolute velocity around the impeller exit section at $t = 92\Delta t$: ———, impeller without the spiral casing; - - - - - -, impeller with the spiral casing; (a) $Q/Q_n = 0{\cdot}47$; (b) $Q/Q_n = 0{\cdot}706$

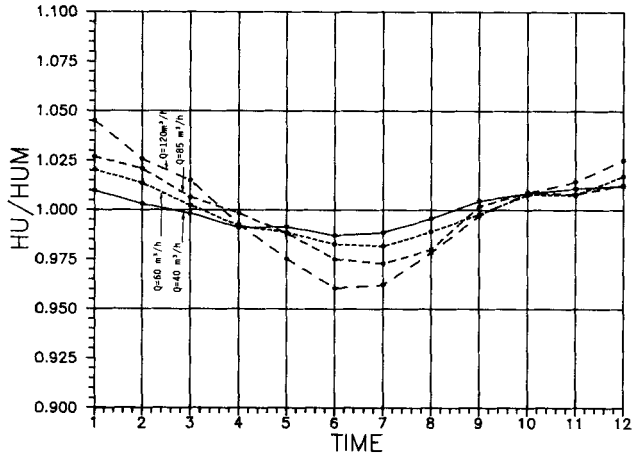

Figure 8. Variation of the theoretical head H_u of the impeller for 12 successive time steps: ———, $Q = 120\ m^3/h$; - - -, $Q = 85\ m^3/h$; - - - -, $Q = 60\ m^3/h$; ———, $Q = 40\ m^3/h$

to 12 time steps. Let H_{um} denote the mean theoretical head obtained during this time interval. In Figure 8 the variation of the ratio H_u/H_{um} is given during a period for the four selected values of the flow rate. At the sixth time step the trailing edge of one blade is located against the tongue. Clearly at this time the developed theoretical head H_u takes its minimum value. Furthermore, it follows from Figure 8 that as the flow rate increases, the variation of H_u becomes more intense.

The mean value H_{um} of the calculated theoretical head of the impeller with and without the spiral casing versus the flow rate Q is plotted in Figure 9. In the same figure the measured total head H of the pump is also plotted. The head H_{um} without the spiral casing is greater than that of the mean head H_{um} of the pump by an almost constant amount, of the order of 0·7 m WG. The difference between the mean theoretical head H_{um} and the measured head H of the pump is due to the hydraulic losses of the flow through the pump. For the selected values of the flow rate the coefficient of hydraulic efficiency, defined as $\eta_h = H/H_{um}$, can be calculated. The overall efficiency η of a centrifugal pump is the product $\eta = \eta_h \eta_Q \eta_m$, where η_Q is the volumetric efficiency and η_m

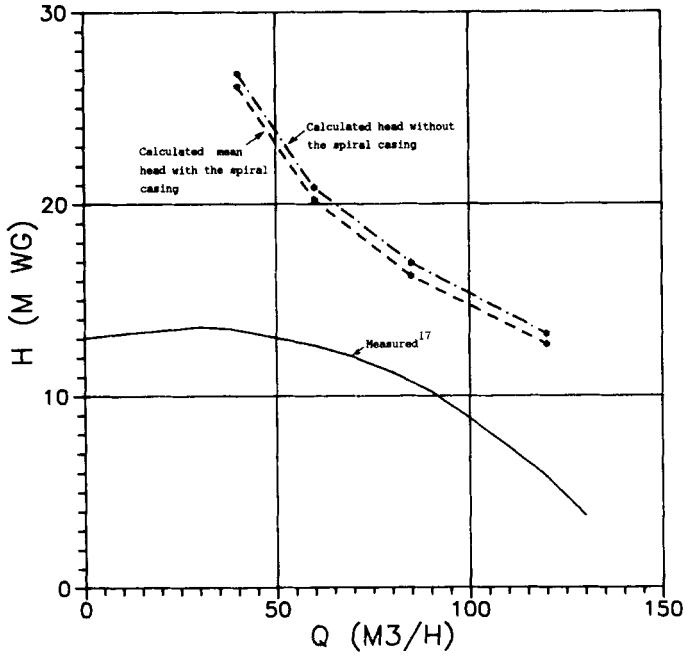

Figure 9. Characteristic curve of the pump running at $n = 1000$ rpm: —·—, calculated head without the spiral casing; – – –, calculated mean head with the spiral casing; ———, measured.[17]

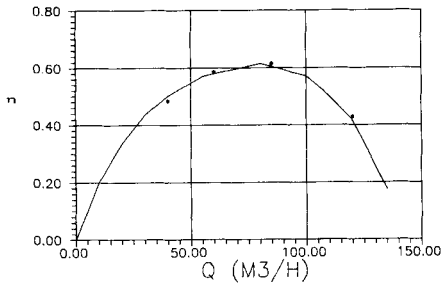

Figure 10. Comparison of the calculated with the measured overall efficiency of the pump running at 1000 rpm: solid line, measured; symbols, calculated

the mechanical efficiency, both of the order of 0·97. The measured values of the overall efficiency η as well as the calculated overall efficiency $\eta_c = \eta_h \eta_Q \eta_m$ versus the flow rate are plotted in Figure 10, proving that the calculated overall performances of the pump are in very good agreement with the corresponding measured values.

CONCLUSIONS

A numerical method based on the theory of unsteady inviscid flow has been developed for the prediction of the unsteady flow established within a radial flow centrifugal pump with a spiral casing. The method has no simplifying assumptions regarding the geometry of either the spiral

casing or the impeller blades. From the results presented it follows that if hydraulic losses are taken into account, the predictions of the head variations are reliable. Regarding the details of the flow field established within the pump (Figures 5 and 6), the patterns produced numerically are at least qualitatively correct. A definite validation would require experimental data not available at the moment and rather difficult to obtain anyway. However, the accuracy of the prediction of the head leads to the conclusion that the method can be used safely as a computational tool for the analysis of pump applications. The procedure could also be applied for the optimization of the spiral casing form and especially of the tongue in order to minimize the disturbances induced in the flow field under off-design operation conditions, thus permitting the reduction of the hydrodynamic noise emitted by the pump.

APPENDIX: NOMENCLATURE

D	physical domain of the flow field
S_i	boundary of the ith blade
S_{wi}	vortex sheet shed from the ith blade
L_0	exit width
L_i	length of S_i
Q	flow rate
ω_R	angular velocity of the impeller
N_b	number of blades
$\mathbf{u}$	velocity field
φ	scalar potential
ψ	streamfunction
ω	vorticity field
σ	surface source distribution
γ	surface vorticity distribution
Γ_i	circulation of the ith blade
γ_{wi}	vorticity shed from the ith blade
$\mathbf{Z}_i$	parametric representation of S_{wi}
Ω_i	intensity of the free vortices
ε	cut-off length
Δt	time step
H	total head developed by the pump
H_u	head ('theoretical') developed by the impeller
c_r	radial component of the absolute velocity
η	efficiency

REFERENCES

1. J. L. Kueny and D. Papantonis, 'Calcul de l'ecoulement instationnaire dans une volute de pompe centrifuge', *XXe Journees d'Hydraulique, SHF, Machines Hydrauliques; Conception et Exploitation*, Lyon, 1989, pp. I.9.1–I.9.10.
2. G. R. Baker, 'The cloud in cell technique applied to the roll up of vortex sheets', *J. Comput. Phys.*, **31**, 76–95 (1979).
3. A. Jolles, 'Resolution des equations de Navier Stokes par des methodes particules maillage', *LIMSI, Notes et Documents, 89-3*, Orsay, 1989.
4. G. Albano, 'Contribution a l'etude des ecoulements internes et instationnaires par la methode des singularités a repartition discretisée', *These de 3e Cycle*, Université de Paris VI, 1979.
5. F. Hureau, 'Mesure et modelisation de l'ecoulement instationnaire dans les pompes centrifuges', *XXe Journees d'Hydraulique, SHF, Machines Hydrauliques; Conception et Exploitation*, SHF, Lyon, 1989, I.14.1–I.14.6.

6. Ph. Devinant, T. Bouet and M. Mudry, 'Modelisation et analyse stationnaires bidimensionnelles de l'ecoulement dans des pompes radiales', *XXe Journees d'Hydraulique, SHF, Machines Hydrauliques; Conception et Exploitation*, Lyon, 1989, I.10.1–I.10.7.
7. H. Shoji and H. Ohashi, 'Lateral fluid forces on whirling centrifugal impeller', *Trans. ASME, J. Fluids Eng.*, **109**, 94–106 (1987).
8. B. C. Basu and G. J. Hancock, 'The unsteady motion of a two-dimensional aerofoil in incompressible inviscid flow', *J. Fluid Mech.*, **87**, 159–178 (1978).
9. D. R. Poling and D. P. Telionis, 'The response of airfoils to periodic disturbances—the unsteady Kutta condition', *AIAA J.*, **24**, 193–199 (1986).
10. J. Katz, 'A discrete vortex method of the non-steady separated flow over an airfoil', *J. Fluid Mech.*, **102**, 315–328 (1981).
11. M. Vezza and R. A. Mcd Galbraith, 'An inviscid model of a steady aerofoil flow with fixed upper surface separation', *Int. j. numer. methods fluids*, **5**, 577–592 (1985).
12. K. W. Mangler and J. H. Smith, 'Behaviour of the vortex sheet at the trailing edge of a lifting wing', *RAE TR 69049*, 1969.
13. A. Mudry, 'La theorie generale des nappes et filaments tourbillonnaires et ses applications a l'aerodynamique instationnaire', *D.E.Sc. Physiques*, Université de Paris VI, 1982.
14. O. H. Hald, 'Convergence of vortex methods for Euler's equations', *SIAM J. Numer. Anal.*, **16**, 726–755 (1979).
15. A. Leonard, 'Vortex methods for flow simulation', *J. Comput. Phys.* **37**, 289–355 (1980).
16. CETIM, 'Etude des efforts hydrodynamiques et des champs de pression, pompe Ns 20', *Rapport Partiel*, Nantes, 1987.
17. R. M. Davino and B. Lakshiminarayana, 'Characteristics of mean velocity in the tip region of turbomachinery rotor exit', *AIAA J.*, **20**, 528–535 (1982).